

Towards quantum supremacy: enhancing quantum control by bootstrapping a quantum processor

Dawei Lu¹, Keren Li^{1,2}, Jun Li³, Hemant Katiyar¹, Annie Jihyun Park^{1,4}, Guanru Feng¹, Tao Xin^{1,2}, Hang Li^{1,2}, GuiLu Long², Aharon Brodutch^{1,5}, Jonathan Baugh¹, Bei Zeng^{1,6} & Raymond Laflamme^{1,7}

¹*Institute for Quantum Computing, University of Waterloo, Waterloo N2L 3G1, Ontario, Canada*

²*State Key Laboratory of Low-Dimensional Quantum Physics and Department of Physics, Tsinghua University, Beijing 100084, China*

³*Beijing Computational Science Research Center, Beijing 100084, China*

⁴*Max-Planck-Institut für Quantenoptik, D-85748 Garching, Germany*

⁵*Center for Quantum Information and Quantum Control, Department of Physics and Department of Electrical and Computer Engineering, University of Toronto, Toronto M5S 3H6, Ontario, Canada*

⁶*Department of Mathematics & Statistics, University of Guelph, Guelph N1G 2W1, Ontario, Canada*

⁷*Perimeter Institute for Theoretical Physics, Waterloo N2L 2Y5, Ontario, Canada*

Quantum computers promise to outperform their classical counterparts in many applications^{1–6}. Rapid experimental progress in the last two decades includes the first demonstrations of small-scale quantum processors⁷, but realising large-scale quantum information processors capable of universal quantum control remains a challenge. One primary obstacle is the inadequacy of classical computers for the task of optimising the experimental control field as

we scale up to large systems⁸. Classical optimisation procedures require a simulation of the quantum system and have a running time that grows exponentially with the number of quantum bits (qubits) in the system. Here we show that it is possible to tackle this problem by using the quantum processor to optimise its own control fields. Using measurement-based quantum feedback control (MQFC)^{9,10}, we created a 12-coherence state with the essential control pulse completely designed by a 12-qubit nuclear magnetic resonance (NMR) quantum processor. The results demonstrate the superiority of MQFC over classical optimisation methods, in both efficiency and accuracy. The time required for MQFC optimisation is linear in the number of qubits, and our 12-qubit system beat a classical computer configured with 2.4 GHz CPU and 8 GB memory. Furthermore, the fidelity of the MQFC-prepared 12-coherence was about 10% better than the best result using classical optimisation, since the feedback approach inherently corrects for unknown imperfections in the quantum processor. As MQFC is readily transferrable to other technologies for universal quantum information processors, we anticipate that this result will open the way to scalably and precisely control quantum systems, bringing us closer to a demonstration of quantum supremacy¹¹.

One of the primary challenges towards building a large-scale universal quantum computer is to achieve sufficient accuracy for quantum error correction⁷. In theory, a complex quantum circuit can be decomposed into elementary gates that work on a restricted number of qubits (usually one or two) and should be readily implemented in experiment¹². In reality however, the control fields are never localised and the qubits interact and evolve even in the absence of the control fields. Consequently the implementation of each elementary gate may require a control sequence

that takes into account a subsystem involving many more than one or two qubits. Moreover, the number of elementary gates required for a quantum algorithm grows polynomially with the system size and the errors accumulate with each successive gate. Therefore, an effective and efficient way to optimise the control field and minimise errors is a key ingredient for scaling up quantum information processing devices¹³.

A second challenge in quantum computing is the demonstration of quantum supremacy¹¹, i.e. building a quantum processor that can significantly outperform classical computers in some task. It is expected that such demonstrations will first be done on a specialised quantum processor, rather than a universal quantum computer, since the former is easier to build. One particular set of tasks where a quantum processor is expected to outperform a classical computer is quantum simulation^{4,5}. Indeed, it is possible to ‘kill two birds with one stone’ by demonstrating quantum supremacy in the task of optimising a quantum control sequence.

Here we take the first steps towards the demonstration of quantum supremacy in a quantum optimisation task by showing that a quantum processor can be used to optimise its own pulses more efficiently and accurately than a classical computer. We use a quantum processor to design a pulse sequence for quantum state engineering. The task is to optimise a control field that will drive the quantum system from a fixed input state ρ_i to a desired target state ρ_f . This problem is important in quantum information processing, as numerous tasks, such as algorithmic cooling in ensemble quantum computing^{14,15}, magic state preparation in fault-tolerant quantum computing¹⁶ and encoding in quantum key distribution¹⁷, all rely on steering states regardless of the propagator. The

gradient ascent pulse engineering (GRAPE) algorithm¹⁸ is the current state-of the-art algorithm to (classically) optimise the control field in quantum state engineering problems. It is widely used in NMR¹⁹, electron spin resonance²⁰, nitrogen-vacancy centres in diamond^{21,22}, superconducting circuits^{23,24}, and ion traps^{25,26}. The GRAPE method exploits the gradient of a fidelity function to update the control field iteratively (Supplemental Information, section 1).

GRAPE has two major drawbacks that are common to all classical optimisation algorithms: its running time is exponential in the size of the n -qubit system, and its accuracy depends on the precision of experimentally obtained parameters describing the quantum system (e.g. the system Hamiltonian). At each iteration k , the algorithm simulates the evolution of the system under the previous pulse, and produces a final state $\tilde{\rho}$ and a fitness function $f = \text{Tr}(\tilde{\rho}\rho_f)$. It then produces a gradient g which is used to correct the pulse. Classically, the computation involves the multiplication of $2^n \times 2^n$ dimensional matrices and takes an exponential (in the number of qubits n) amount of time. For instance, a cluster of 128 AMD *Opteron 850* CPU (2.4 GHz) can only handle a problem size of about ten qubits using GRAPE⁸.

While it is clear that a universal quantum computer can be used to simulate the evolution efficiently, one could ask if a less powerful quantum machine could be used to calculate f and g efficiently. Recently, this question has been answered affirmatively^{9,10}. A technique called measurement-based quantum feedback control (MQFC) enables direct measurement of f and g (see Fig. 1a). MQFC uses the quantum processor to optimise its own pulses, addressing both the issue of scalability (e.g., see Fig. 1b for the running time comparison between MQFC on an NMR

quantum processor and GRAPE on classical computers), as well as control inaccuracies due to imperfect system characterisation^{27,28}.

Here we report a 12-qubit experiment on an NMR quantum processor, which exhibits both of the above advantages of MQFC. It is worth emphasising that the MQFC method is general, and is readily transferrable to any implementation in which control fields steer the system evolution and measurement in a standard basis is possible. To begin, let us clarify two points in our experimental description to avoid confusion. First, all pulses except the MQFC pulse throughout our experiments are generated by a subsystem-based GRAPE (SSGRAPE) approach¹⁹, and result in local rotations. Note that SSGrAPE is a technical improvement of GRAPE for our particular implementation, but does not address its scalability issue (see Methods). No 2^{12} -dimensional classical optimisations were performed in the course of this work. Second, we refer to unnormalised deviation density matrices (without the identity term) as 'states', which is a standard convention in ensemble quantum computing.

In our NMR quantum processor, the 12 qubits are denoted by nuclear spins C₁ to C₇ (¹³C-labeled) for qubits 1 to 7, and H₁ to H₅ for qubits 8 to 12 in the molecule shown by Fig. 2a. It has a rotating-frame system Hamiltonian with σ_z terms resulting from the spin Zeeman interaction and $\sigma_z\sigma_z$ terms resulting from the isotropic coupling in a static magnetic field (see Methods). The transverse control field is applied in the *x*-*y* plane, which is digitised into M slices with slice length Δt . In each slice, the four parameters of the control field are constants, leading to a control

Hamiltonian

$$\mathcal{H}_c[m] = B_x^C[m] \sum_{i=1}^7 \sigma_x^i + B_y^C[m] \sum_{i=1}^7 \sigma_y^i + B_x^H[m] \sum_{j=8}^{12} \sigma_x^j + B_y^H[m] \sum_{j=8}^{12} \sigma_y^j, \quad (1)$$

where, for example, $B_x^C[m]$ means the control field amplitude along the rotating-frame x -axis for the ^{13}C channel in slice m .

The dynamics of the NMR system is determined by \mathcal{H}_s and \mathcal{H}_c simultaneously, with the propagator

$$U_{[1]}^{[M]} = U_M U_{M-1} \cdots U_1, \quad \text{with} \quad U_m = e^{-i(\mathcal{H}_s + \mathcal{H}_c[m])\Delta t}. \quad (2)$$

The essence of NMR quantum information processing is to optimise a control field, i.e. find a sequence of $B_{x,y}^{\text{C,H}}[m]$, such that one can precisely realise a quantum gate or drive the system to a target state according to Eq. (2).

As mentioned above, GRAPE is a powerful tool to achieve this optimisation, but optimising over the whole system of n qubits is not scalable. Taking our experiment as an example, finding a control field that evolves single-coherence $ZI^{\otimes 11}$ to 12-coherence $Z^{\otimes 12}$ (we use capital Z to denote states and σ_z to denote Hamiltonians, while they both refer to the same Pauli-z matrix) is near the limit of capability for a typical desktop computer using GRAPE (see Fig. 1b). In contrast, MQFC is able to solve this control problem in a time that scales linearly with the number of qubits, as shown in the following experiment. The entire experimental procedure is depicted in Fig. 2c, with a step-by-step description in Supplemental Information, section 4 and 5.

First, we prepare 7-coherence $Z^{\otimes 7}I^{\otimes 5}$ on seven ^{13}C spins, using the sequence in Fig. 2c

before the *MQFC optimisation* box. This procedure, benchmarked in our previous work ²⁹, is mainly done with the aid of SSGRAPE. Subsequently, we create $Z^{\otimes 12}$ via MQFC optimisation on the quantum processor, which is the main focus of this work. We attempt to optimise a control field, namely a shaped radio frequency (r.f.) pulse, to evolve the system from the input $\rho_i = Z^{\otimes 7}I^{\otimes 5}$ to the output $\rho_f = Z^{\otimes 12}$ via MQFC. Our control field, as shown in the *MQFC optimisation* box, is comprised of three sub-pulses to realise local rotations, and two free evolutions to let ¹³C qubits interact with ¹H qubits for the purpose of generating higher coherence. The whole control field is digitised into $M = 278$ slices with $\Delta t = 20 \mu\text{s}$ width, while 110 slices are for three sub-pulses and 168 slices remain zero to realise the two 1.68 ms free evolutions. The dynamics is given by $U_{[1]}^{[M]}$ in Eq. (2).

The fitness function is defined as $f = \text{tr}(\rho_f \tilde{\rho})$, a metric for the control fidelity, where $\tilde{\rho} = U_{[1]}^{[M]} \rho_i U_{[1]}^{[M]\dagger}$ is the experimental state and $\rho_f = Z^{\otimes 12}$ is the target. In our experiment, only one measurement of the expectation value of $\langle Z^{\otimes 12} \rangle$ suffices to attain f after each iteration. If f does not hit our preset value with the current control field, we navigate the control field along its gradient g . In fact, to measure $g_x[m]$ which is the gradient of slice m , we just need three steps: insert a local $\pm\pi/2$ pulse on every qubit about x -axis between slice m and $m + 1$; apply this new control field to the initial state ρ_i and measure f ; compute $g_x[m]$ by directly combining these $\pm\pi/2$ -inserted results (see Fig. 2b and Methods). As long as accurate local $\pm\pi/2$ pulses are available for each qubit, g can be measured on a quantum processor. In experiment we have designed a 1 ms $\pi/2$ pulse on every ¹³C nucleus with the simulated fidelity over 99.7%. Having the gradient, we can update the control field and continue the MQFC procedure until a desired f is attained.

Figure 3a shows the spectrum corresponding to the 12-coherence after the MQFC optimisation, where C_7 is the probe qubit. After rescaling the experimental result by 1.21 times to compensate for decoherence, it fits the simulation very well, which indicates that $Z^{\otimes 12}$ is faithfully created. This is the first direction observation of a coherence order >10 in terms of one-dimensional spectrum in NMR spectroscopy, which requires all couplings between the probe spin and other spins to be well resolved. Figure 3b shows the spectrum of $\tilde{\rho}$ after the readout stage for each odd iteration. The peak intensities correspond to the value of $f = \text{tr}(Z^{\otimes 12}\tilde{\rho})$, which clearly shows that MQFC increases f during the optimisation. This demonstrates that MQFC is a practical technique for designing control fields in large quantum systems.

Now we analyse the time complexity and performance of the MQFC approach. With respect to time complexity, we need one experiment to measure f and $4nM$ experiments to measure g for each iteration, where n is the number of qubits. Assume each experiment takes τ_{exp} time, the MQFC in total consumes $T_{exp} = (4nM + 1)\tau_{exp}$ for each iteration. By contrast, one has to deal with massive 2^n -dimensional matrix multiplications and exponentials using GRAPE on a classical computer. Figure 1b shows the comparison of the running time for one iteration between MQFC on an NMR quantum processor and GRAPE on classical computers with different configurations. In the 12-qubit scenario, the quantum processor has already outperformed the classical computer with 8 GB memory in regard to memory.

Beyond superior scalability, our experiment also exhibits MQFC's ability of correcting experimental errors. To demonstrate this improvement, we implement another set of 12-coherence-

creating experiments but using classical SSGRAPE methods. Figure 3c illustrates the result of SS-GRAPE and MQFC pulses both in simulation and experiment. Focusing on the final result at iteration 9 in Fig. 3d, in experiment SS GRAPE finally creates a 12-coherence with $f = 0.703 \pm 0.034$, whereas MQFC pulse creates $f = 0.795 \pm 0.027$. This experimental improvement of nearly 10% disagrees with simulation, as in simulation MQFC (0.830) is worse than SS GRAPE (0.931). Considering that MQFC is a feedback-control process, some incomplete knowledge of the experimental quantum process, such as the nonlinearity of the pulse generator or imprecision of the molecular Hamiltonian, may lead to this inconsistency. Therefore, the experiment suggests that MQFC is indeed advantageous with respect to correcting errors from unknown sources. Furthermore, we simulated the decoherence effect during the procedure of creating 12-coherence, and found that the upper bound of $\text{tr}(Z^{\otimes 12} \tilde{\rho})$ in the presence of dephasing noise is about 0.824 (see Methods). Our MQFC result reaches 0.795, which is very close to this bound, demonstrating that our control of this 12-qubit processor is close to the theoretical prediction after accounting for decoherence.

In summary, we create 12-coherence on an NMR quantum processor using MQFC. Our experimental procedure and result, in particular the direct observation of 12-coherence with one qubit as the probe, signify the capability of our quantum processor to serve as a universal 12-qubit quantum processor with high-fidelity individual controls on each qubit. In terms of control field optimisation, our experiment demonstrates two superiorities in efficiency and experimental performance of MQFC beyond its classical counterpart. MQFC requires a running time that scales linearly with the number of qubits, and yields about 10% improvement compared to the best result

via classical optimisation. Notably, this experiment already outperforms a modern classical computer in the task of creating the 12-coherence state, indicating that our experiment is a significant step towards quantum supremacy. The dominating factor that limits our MQFC optimisation is the long wait time (about $5T_1 \approx 30$ s) between experiments to reinitialise the quantum processor, other systems such as superconducting circuits or nitrogen-vacancy centres in diamond with much shorter T_1 may circumvent this obstacle. Hence, the running time of MQFC promises to be remarkably faster in these systems, so that even fewer qubits will be needed to outperform classical optimisation. As nine qubits can be reliably manipulated with state-of-the-art techniques³⁰, we anticipate to witness quantum supremacy in the near future.

Methods

Experimental setup. Our experiments were carried out at room temperature on a Bruker Avance 700 MHz DRX spectrometer. The liquid-state sample is per-¹³C labeled (1S,4S,5S)-7,7-dichloro-6-oxo-2-thiabicyclo[3.2.0]heptane-4-carboxylic acid dissolved in d6-acetone, which forms a 12-qubit register. When placed in a static z -magnetic field, it has an systematic Hamiltonian of Ising-model, with the form

$$\mathcal{H}_s = -\pi \sum_{i=1}^{12} \nu_0^i \sigma_z^i + \frac{\pi}{2} \sum_{i=1 < j}^{12} J_{ij} \sigma_z^i \sigma_z^j, \quad (3)$$

where ν_0^i is the Larmor frequency of the i th qubit, J_{ij} is the coupling between qubits i and j , and σ_z^i is the Pauli-z operator of the i th qubit.

Typical lengths of the local operations are 1 ms for $\pi/2$ rotations and 2 ms for π rotations, with all simulated fidelities over 99.7%. Prior to the implementation of 12-coherence creation, we

boost the signal of C₇ via a nuclear Overhauser effect (NOE)-induced 8 ms partial-SWAP gate as shown in Fig. 2c. This step enhances approximately 3.7 times of C₇ signal using the fact that the gyromagnetic ratio of ¹H is 3.98 times larger than that of ¹³C, and hence improves the signal-to-noise ratio for the oncoming experiments. The timescale to initialise our NMR system back to the thermal equilibrium is about 30 s, which is the primary factor that limits our experimental time per run.

SSGRAPE. First of all, SSGrApe is still classical, and cannot address the scalability issues of GRAPE ¹⁹. Even though, SSGrApe is an important modification to the original GRAPE algorithm, which can improve the timescale of calculating GRAPE pulses dramatically by defining subsystems based on the Hamiltonian of the molecule. For instance, in our 12-qubit molecule, we define two 6-qubit subsystems by detaching C₂ from C₇, which reduces the computing complexity greatly. Such a separation is optimal in this particular molecule, as the sole remarkable connection between the two subsystems is the coupling between C₂ and C₇. Thereafter, the total fitness function f can be written as a sum of fitness functions of subsystems, as long as the target operation does not involve communications between subsystems. From Fig. 2c, we know that all intended operations in our experiment are local, implying that we can apply SSGrApe to calculate each operation in principle. Again, SSGrApe vastly relies on the molecular structure and the operations to be optimised, leading to its scalability similar to the original GRAPE algorithm.

Measurement of f and g . Both in GRAPE and MQFC algorithm, the metric to evaluate the control fidelity is defined as

$$f = \text{tr}(\tilde{\rho}\rho_f) = \text{tr}\left(\mathbf{U}_{[1]}^{[M]}\rho_i\mathbf{U}_{[1]}^{[M]\dagger}\cdot\rho_f\right), \quad (4)$$

where $\tilde{\rho}$ is the experimentally prepared state, ρ_f is the target, and $\mathbf{U}_{[1]}^{[M]} = \mathbf{U}_M\mathbf{U}_{M-1}\cdots\mathbf{U}_1$ describes the dynamics of the system. It returns one if and only if $\tilde{\rho}$ equals to ρ_f . To implement MQFC on a quantum processor, f should be efficiently measured without state tomography on $\tilde{\rho}$. When ρ_f is simple, e.g. only a few non-zero components when it is decomposed in the computational basis for non-ensemble systems, or decomposed in Pauli basis for ensemble systems. In this case, one just needs to measure those non-zero components in $\tilde{\rho}$ to compute f instead of carrying out full state tomography (Supplemental Information, section 2). For instance, in our experiment only one measurement, namely the expectation value of

$$\langle Z^{\otimes 12} \rangle = \text{tr}(Z^{\otimes 12}\tilde{\rho}), \quad (5)$$

suffices to attain f after each iteration.

To find the optimum of f , we calculate its gradient to the first order when Δt is small. In fact, for the m th slice of the control field, g can be expanded as (Supplemental Information, section 2)

$$\begin{aligned} g_{x,y}[m] &= \frac{\partial f}{\partial \mathbf{B}_{x,y}[m]} \approx \sum_{k=1}^n \text{tr}\left(-i\Delta t \mathbf{U}_{[m+1]}^{[M]} \left[\sigma_{x,y}^k, \mathbf{U}_{[1]}^{[m]}\rho_i\mathbf{U}_{[1]}^{[m]\dagger}\right] \mathbf{U}_{[m+1]}^{[M]\dagger}\cdot\rho_f\right) \\ &= \sum_{i=1}^n \frac{\Delta t}{2} \text{tr}\left\{ \left[\mathbf{U}_{[m+1]}^{[M]} \left(\frac{\pi}{2}\right)_{x,y}^i \mathbf{U}_{[1]}^{[m]}\rho_i\mathbf{U}_{[1]}^{[m]\dagger} \left(\frac{\pi}{2}\right)_{x,y}^{i\dagger} \mathbf{U}_{[m+1]}^{[M]\dagger} \right. \right. \\ &\quad \left. \left. - \mathbf{U}_{[m+1]}^{[M]} \left(-\frac{\pi}{2}\right)_{x,y}^i \mathbf{U}_{[1]}^{[m]}\rho_i\mathbf{U}_{[1]}^{[m]\dagger} \left(-\frac{\pi}{2}\right)_{x,y}^{i\dagger} \mathbf{U}_{[m+1]}^{[M]\dagger} \right] \cdot \rho_f \right\}, \end{aligned} \quad (6)$$

where $(\pi/2)_{x,y}^i$ represents a $\pi/2$ rotation about $x(y)$ -axis for qubit i . The final expression of g , if focusing on each term, is very similar to the measurement of f , where the sole difference is the insertion of a local $\pm\pi/2$ pulse between slices m and $m + 1$. Therefore, say to measure $g_x[m]$, $2n$ experiments are needed assuming that f can be measured in one run, which is the case in our 12-coherence creating experiment. It proceeds as: insert $(\pm\pi/2)_x^i$ at the m -th slice evolution, apply this $\pi/2$ -inserted control field, measure the relevant f , and combine the $2n$ results according to Eq. (6). Measuring $g_y[m]$ is analogous.

Noting that the circuit in the *MQFC optimisation* box of Fig. 2c involves no local operations on ${}^1\text{H}$ qubits, we further simplify the measurement of g by applying $\pm\pi/2$ pulses on seven ${}^{13}\text{C}$ qubits only. Additionally, the 168-slice free evolutions in the control field remain zero during optimisation, so they do not require the measurement of g either, which further reduces our experimental time.

Observation of 12-coherence. In NMR spectroscopy, multiple coherence is hard to be observed directly in a one-dimensional spectrum, i.e., by flipping the target spin to the x - y plane while others remain in Z . If all coupling between the target spin and other spins can be resolved, such observation is feasible. For example, in a two-qubit system, we can flip spin one to X to observe ZZ . In fact, XZ can be written as

$$XZ = X \otimes |0\rangle\langle 0| - X \otimes |1\rangle\langle 1|. \quad (7)$$

The first term $X \otimes |0\rangle\langle 0|$ leads to a positive peak at $\nu_1 - J_{12}/2$ in the spectrum, as the J -coupling term shifts the frequency of qubit 1 by $-J_{12}/2$. Analogously, the second term $X \otimes |1\rangle\langle 1|$ leads to a

negative (note the minus sign before the term) peak at $\nu_1 + J_{12}/2$. Generally, these two peaks can be resolved in the spectrum as long as J is large enough to separate the above two frequencies. However, to observe multiple coherence, this requirement is of great challenge, since all J -couplings between the target spin and other spins should be sufficiently large to prevent the annihilations of positive and negative peaks. As a result, two-dimensional spectra and special techniques are usually employed to observe multiple coherence in conventional NMR spectroscopy.

For the purpose of NMR quantum computing, it is certainly better to read out multiple coherence directly in a one-dimensional spectrum, as one-dimensional spectrum reflects the state information more intuitively and reduces running time remarkably compared to two-dimensional spectroscopy. In our 12-qubit processor, although there are a few couplings as small as 0.01 Hz (Supplemental Information, section 3), the direct observation of 12-coherence $Z^{\otimes 12}$ is still available on C_7 . Figure 3a exhibits a strong agreement between experimental observation 12-coherence with merely 32 number of scans and the simulation. To our best knowledge, our experiment is the first direct observation of multiple coherence beyond ten spins, and provides a valid evidence that our 12-qubit processor possesses excellent individual controllability and the potential to be a universal 12-qubit quantum processor.

Decoherence simulation. To numerically simulate the decoherence effect in our 12-qubit system, we first make the following assumptions: the environment is Markovian; only the T_2^* dephasing mechanism is taken into account since T_1 effect is negligible in our circuit; the dephasing noise is independent between all qubits; the dissipator and the total Hamiltonian commute in each pulse slice as $\Delta t = 20 \mu\text{s}$ is small. With these assumptions, we solve the master equation in two steps

for each Δt : evolve the system by the propagator in Eq. (2), and subsequently apply the dephasing noise for Δt which is an exponential decay of off-diagonal elements in the density matrix. The typical length of simulating our 12-qubit experiment in the presence of dephasing noise is in the magnitude of days on a desktop computer. The simulation shows that at most $F_{dec} = 0.824$ of $Z^{\otimes 12}$ can be achieved with the 5.56 ms MQFC pulse applied on $Z^{\otimes 7}I^{\otimes 5}$, which is reasonable as high-order coherence is very vulnerable to the dephasing noise. Alternatively speaking, the upper bound of the MQFC experimental result is 0.824, since the optimisation procedure does not include the function of robustness against dephasing noise yet.

References

1. Shor, P. W. Algorithms for quantum computation: Discrete logarithms and factoring. In *Foundations of Computer Science, 1994 Proceedings., 35th Annual Symposium on*, 124–134 (IEEE, 1994).
2. Grover, L. K. A fast quantum mechanical algorithm for database search. In *Proceedings of the twenty-eighth annual ACM symposium on Theory of computing*, 212–219 (ACM, 1996).
3. Farhi, E. *et al.* A quantum adiabatic evolution algorithm applied to random instances of an np-complete problem. *Science* **292**, 472–475 (2001).
4. Buluta, I. & Nori, F. Quantum simulators. *Science* **326**, 108–111 (2009).
5. Georgescu, I., Ashhab, S. & Nori, F. Quantum simulation. *Rev. Mod. Phys.* **86**, 153 (2014).

6. Harrow, A. W., Hassidim, A. & Lloyd, S. Quantum algorithm for linear systems of equations. *Phys. Rev. Lett.* **103**, 150502 (2009).
7. Ladd, T. D. *et al.* Quantum computers. *Nature* **464**, 45–53 (2010).
8. Gradl, T., Spörl, A., Huckle, T., Glaser, S. J. & Schulte-Herbrüggen, T. Parallelising matrix operations on clusters for an optimal control-based quantum compiler. In *European Conference on Parallel Processing*, 751–762 (Springer, 2006).
9. Li, J., Yang, X., Peng, X. & Sun, C.-P. Physical realization of a quantum oracle machine. *arXiv:1608.00677* (2016).
10. Rebentrost, P., Schuld, M., Petruccione, F. & Lloyd, S. Quantum gradient descent and newton’s method for constrained polynomial optimization. *arXiv:1612.01789* (2016).
11. Preskill, J. Quantum computing and the entanglement frontier. *arXiv:1203.5813* (2012).
12. Nielsen, M. A. & Chuang, I. L. *Quantum computation and quantum information* (Cambridge university press, 2010).
13. Brif, C., Chakrabarti, R. & Rabitz, H. Control of quantum phenomena: past, present and future. *New J. Phys.* **12**, 075008 (2010).
14. Boykin, P. O., Mor, T., Roychowdhury, V., Vatan, F. & Vrijen, R. Algorithmic cooling and scalable nmr quantum computers. *Proc. Natl. Acad. Sci. USA* **99**, 3388–3393 (2002).

15. Baugh, J., Moussa, O., Ryan, C. A., Nayak, A. & Laflamme, R. Experimental implementation of heat-bath algorithmic cooling using solid-state nuclear magnetic resonance. *Nature* **438**, 470–473 (2005).
16. Souza, A. M., Zhang, J., Ryan, C. A. & Laflamme, R. Experimental magic state distillation for fault-tolerant quantum computing. *Nat. Commun.* **2**, 169 (2011).
17. Bennett, C. H. Quantum cryptography: Public key distribution and coin tossing. In *International Conference on Computer System and Signal Processing, IEEE, 1984*, 175–179 (1984).
18. Khaneja, N., Reiss, T., Kehlet, C., Schulte-Herbrüggen, T. & Glaser, S. J. Optimal control of coupled spin dynamics: design of nmr pulse sequences by gradient ascent algorithms. *J. Magn. Reson.* **172**, 296–305 (2005).
19. Ryan, C., Negrevergne, C., Laforest, M., Knill, E. & Laflamme, R. Liquid-state nuclear magnetic resonance as a testbed for developing quantum control methods. *Phys. Rev. A* **78**, 012328 (2008).
20. Zhang, Y., Ryan, C. A., Laflamme, R. & Baugh, J. Coherent control of two nuclear spins using the anisotropic hyperfine interaction. *Phys. Rev. Lett.* **107**, 170503 (2011).
21. Waldherr, G. *et al.* Quantum error correction in a solid-state hybrid spin register. *Nature* **506**, 204–207 (2014).
22. Dolde, F. *et al.* High-fidelity spin entanglement using optimal control. *Nat. Commun.* **5** (2014).

23. Motzoi, F., Gambetta, J., Rebentrost, P. & Wilhelm, F. K. Simple pulses for elimination of leakage in weakly nonlinear qubits. *Phys. Rev. Lett.* **103**, 110501 (2009).
24. Egger, D. J. & Wilhelm, F. K. Optimized controlled-z gates for two superconducting qubits coupled through a resonator. *Supercond. Sci. Technol.* **27**, 014001 (2013).
25. Nebendahl, V., Häffner, H. & Roos, C. Optimal control of entangling operations for trapped-ion quantum computing. *Phys. Rev. A* **79**, 012312 (2009).
26. Schindler, P. *et al.* Experimental repetitive quantum error correction. *Science* **332**, 1059–1061 (2011).
27. Vijay, R. *et al.* Stabilizing rabi oscillations in a superconducting qubit using quantum feedback. *Nature* **490**, 77–80 (2012).
28. Hirose, M. & Cappellaro, P. Coherent feedback control of a single qubit in diamond. *Nature* **532**, 77–80 (2016).
29. Lu, D. *et al.* Experimental estimation of average fidelity of a clifford gate on a 7-qubit quantum processor. *Phys. Rev. Lett.* **114**, 140505 (2015).
30. Kelly, J. *et al.* State preservation by repetitive error detection in a superconducting quantum circuit. *Nature* **519**, 66–69 (2015).

Supplementary Information is available in the online version of the paper.

Acknowledgements We thank Anthony P. Krismanich, Ahmad Ghavami, and Gary I. Dmitrienko for synthesising the NMR sample. This research was supported by CIFAR, NSERC and Industry of Canada. K.L., H.L. and G.L. acknowledge National Natural Science Foundation of China under Grants No. 11175094 and No. 91221205.

Author Contributions D.L., J.L. and R.L. conceived the experiments. D.L. and K.L. performed the experiment and analysed the data. D.L., H.K., A.P., G.F. and H.L. tested the sample and developed the control techniques. J.L. and A.B. provided theoretical support. G.L., J.B., B.Z. and R.L. supervised the project. D.L., K.L. and J.L. wrote the manuscript with feedback from all authors.

Author Information The authors declare that they have no competing financial interests. Correspondence and requests for materials should be addressed to D.L. (d29lu@uwaterloo.ca) or K.L. (lkr14@mails.tsinghua.edu.cn).

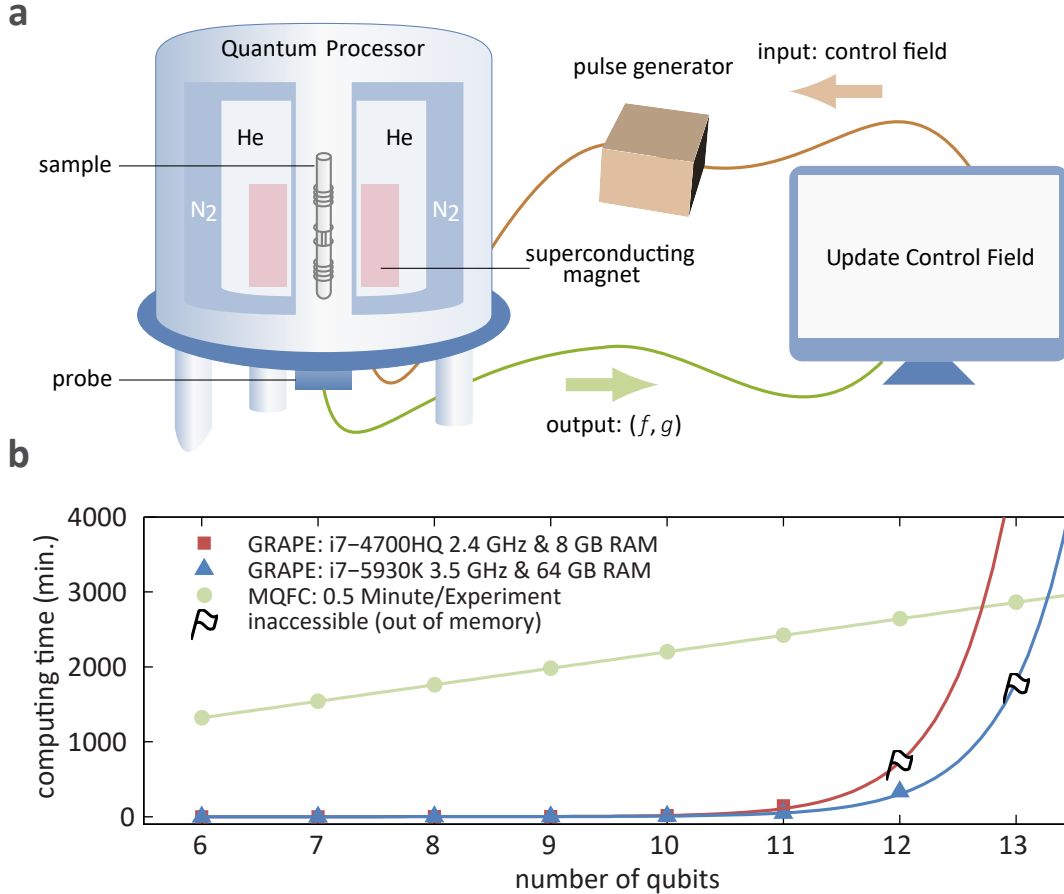


Figure 1: Schematic diagram of MQFC and its time complexity. **a**, MQFC process for optimising a control field. Starting from an initial guess, a shaped pulse is created from the pulse generator and then applied to the sample. f and g are directly measured on the quantum processor, where g is used to update the control field until the objective f is satisfactorily achieved. **b**, We test GRAPE optimisations using two classical computers with different configurations, and compare their running time with the MQFC procedure on an NMR quantum processor. Obviously, GRAPE optimisation takes exponential time, i.e. not scalable with the number of qubits, whereas MQFC is only linear. In particular, the lower-configured classical computer cannot tackle 12 qubits, which is the case in this work, due to the memory issue.

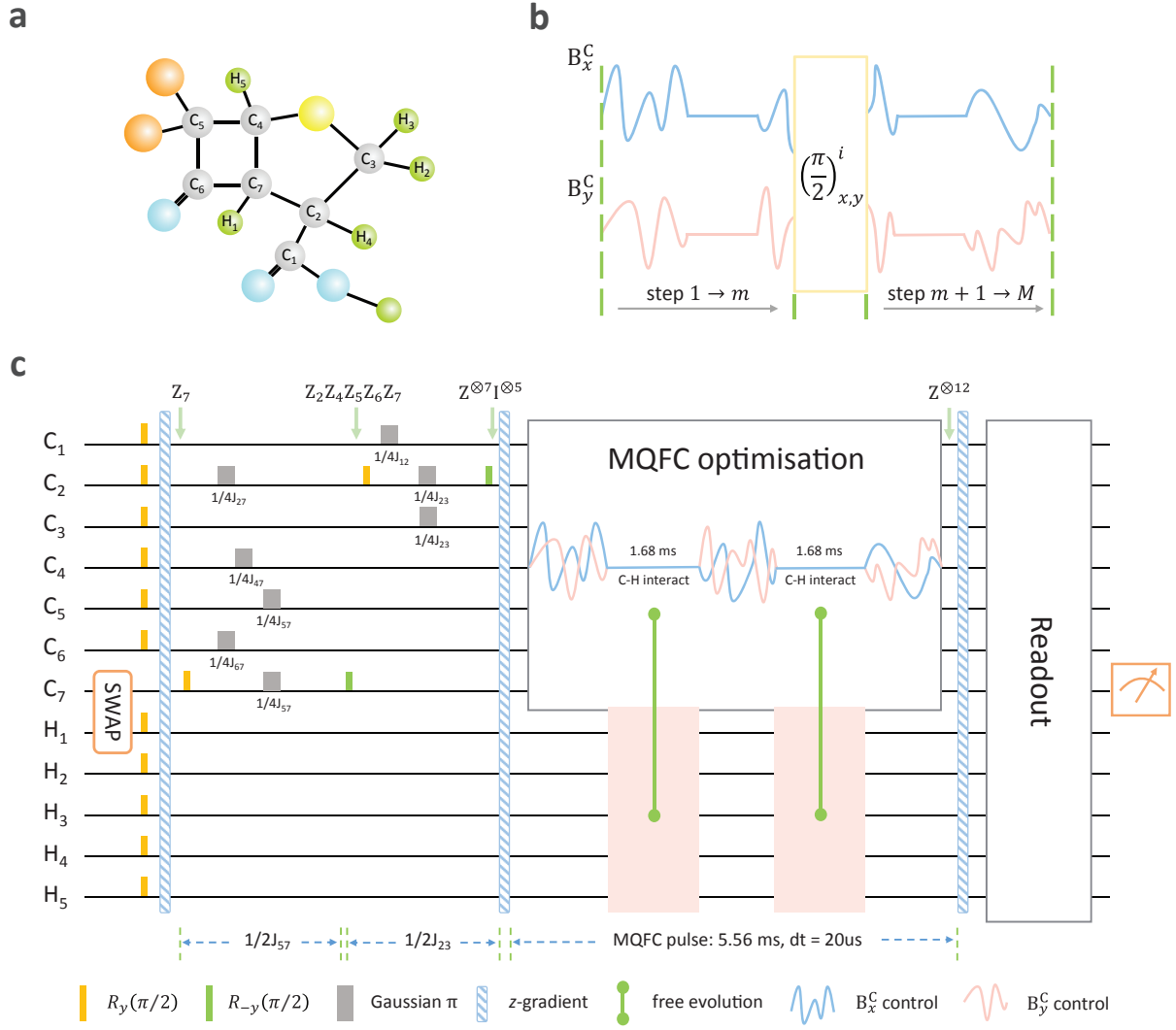


Figure 2: MQFC scheme in creating 12-coherence. **a**, Molecular structure of the 12-qubit quantum processor. **b**, Schematic of measuring the m -th step gradient $g_{x,y}[m]$. A $\pi/2$ rotation about $x(y)$ -axis for qubit i is inserted between the m -th and $(m + 1)$ -th slices (see Methods). **c**, Quantum circuit that evolves the system from the thermal equilibrium to 12-coherence, where MQFC is applied on 7-coherence $Z^{\otimes 7}I^{\otimes 5}$.

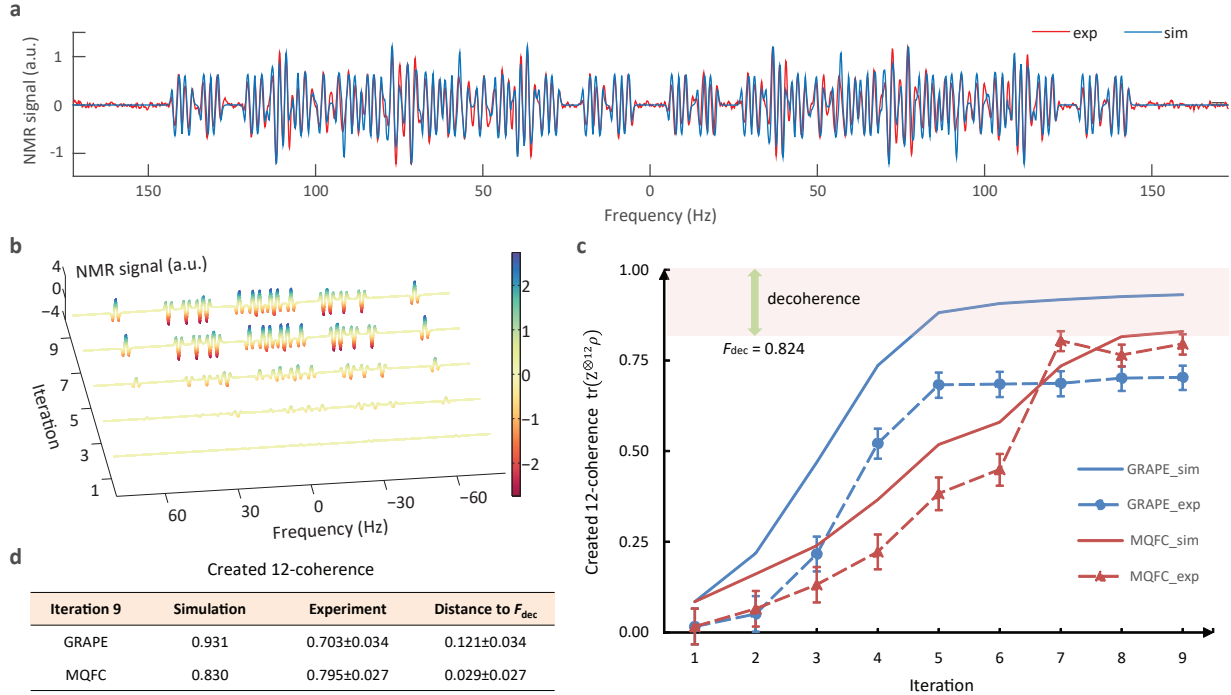


Figure 3: Experimentally created 12-coherence using MQFC. **a**, Direct observation of the created 12-coherence in one-dimensional NMR spectrum (red), where C₇ is the probe qubit. Simulated spectrum (blue) is also plotted. The experimental result is rescaled by 1.21 times to compensate for the decoherence effect for better visualisation. **b**, Spectra of 12-coherence after each odd iteration during the MQFC optimisation. Unlike **a**, a readout technique (Supplemental Information, section 6) is applied to gain a higher resolution. A colour scale indicates peak intensities. The height of the peaks is proportional to the value of created 12-coherence. **c**, Comparison between GRAPE (blue) and MQFC (red) optimisations, both in simulation (solid; without decoherence accounted) and experiment (dashed). F_{dec} is the numerical simulation of decoherence during the 12-coherence creation. Compared to the GRAPE algorithm, MQFC optimisation is worse in simulation, but better in experiment. The error bars are plotted by the infidelity of the readout pulse. **d**, Results at iteration 9. The experimental 12-coherence reaches 0.795 using MQFC which approaches the $F_{dec} = 0.824$ bound, while GRAPE only leads to 0.703 (0.121 lower than F_{dec}) in experiment.

Supplemental information for "Towards quantum supremacy: enhancing quantum control by bootstrapping a quantum processor"

Dawei Lu,^{1,*} Keren Li,^{1,2,†} Jun Li,³ Hemant Katiyar,¹ Annie Jihyun Park,^{1,4} Guanru Feng,¹ Tao Xin,^{1,2} Hang Li,^{1,2} Guilu Long,² Aharon Brodutch,^{1,5} Jonathan Baugh,¹ Bei Zeng,^{1,6} and Raymond Laflamme^{1,7}

¹*Institute for Quantum Computing, University of Waterloo, Waterloo N2L 3G1, Ontario, Canada*

²*State Key Laboratory of Low-Dimensional Quantum Physics and Department of Physics, Tsinghua University, Beijing 100084, China*

³*Beijing Computational Science Research Center, Beijing 100084, China*

⁴*Max-Planck-Institut für Quantenoptik, D-85748 Garching, Germany*

⁵*Center for Quantum Information and Quantum Control,
Department of Physics and Department of Electrical and Computer Engineering,
University of Toronto, Toronto M5S 3H6, Ontario, Canada*

⁶*Department of Mathematics & Statistics, University of Guelph, Guelph, Ontario, Canada*

⁷*Perimeter Institute for Theoretical Physics, Waterloo N2L 2Y5, Ontario, Canada*

1. Fundamentals of the GRAPE algorithm

The GRAPE algorithm [1] is developed for the design of optimal control pulses in NMR spectroscopy. Here, we explain the basic principle of GRAPE by considering the problem of state engineering in the absence of relaxation. Suppose the initial state of the spin system is ρ_i , and the target output state is ρ_f . If the input transverse control field is digitised as a sequence $(\mathbf{B}_x[m], \mathbf{B}_y[m])$, where $m = 1, \dots, M$ denotes the m th time step, the system will evolve into the following state

$$\tilde{\rho} = U_M U_{M-1} \cdots U_1 \rho_i U_1^\dagger \cdots U_{M-1}^\dagger U_M^\dagger, \quad (1)$$

after applying this pulse. Here, $U_m = e^{-i(\mathcal{H}_s + \mathcal{H}_c[m])\Delta t}$ with Δt being the time length of each time slice. The fitness function defined as $f = \text{tr}(\rho_f \tilde{\rho})$ serves as a metric for the control fidelity, with the form

$$f = \text{tr}(\rho_f \tilde{\rho}) = \text{tr}\left(U_M U_{M-1} \cdots U_1 \rho_i U_1^\dagger \cdots U_{M-1}^\dagger U_M^\dagger \cdot \rho_f\right). \quad (2)$$

Clearly, f is a function of $2M$ variables, and to find its optimum we calculate the gradient function to the first order

$$g_{x,y}[m] = \frac{\partial f}{\partial \mathbf{B}_{x,y}[m]} \approx \sum_{k=1}^n \text{tr}\left(-i\Delta t U_M \cdots U_{m+1} \left[\sigma_{x,y}^k, U_m \cdots U_1 \rho_i U_1^\dagger \cdots U_m^\dagger\right] U_{m+1}^\dagger \cdots U_M^\dagger \rho_f\right). \quad (3)$$

We may increase the fitness function f if we use the gradient iteration rule

$$\mathbf{B}_{x,y}[m] \leftarrow \mathbf{B}_{x,y}[m] + \epsilon \cdot g_{x,y}[m]. \quad (4)$$

where ϵ is a suitably chosen step size.

The GRAPE algorithm proceeds as follows on a classical computer:

- (i) start from an initial guess control $(\mathbf{B}_x[m], \mathbf{B}_y[m])$;
- (ii) calculate $\tilde{\rho}$ according to Eq. (1);
- (iii) evaluate fitness function $f = \text{tr}(\rho_f \tilde{\rho})$;
- (iv) if f does not reach our preset value, evaluate gradient function g according to Eq. (3);
- (v) update control variables according to Eq. (4), then go to step (ii).

* d29lu@uwaterloo.ca

† lkr14@mails.tsinghua.edu.cn

2. Measurement of f and g using the MQFC scheme

MQFC is still a gradient-based optimisation, where the essential point is to realise the estimation of f and g through the process of quantum evolution and quantum measurement. Without loss of generality, here we discuss the scenario of ensemble quantum computing, where the state is usually written as a traceless deviation density matrix. For other systems which use the computational $|0\rangle$ and $|1\rangle$ basis, the following procedure just needs to be slightly modified.

Measuring f is straightforward. If the target state ρ_f has some decomposition that $\rho_f = \sum_{r=1}^R x_r P_r$ with respect to the Pauli basis, then

$$f = \text{tr}(\tilde{\rho}\rho_f) = \sum_{r=1}^R x_r \text{tr}(\tilde{\rho}P_r), \quad (5)$$

where $1 \leq R \leq 4^n$ depends on the form of ρ_f , P_r is an operator in the Pauli group, and x_r is its corresponding coefficient. For a n -qubit system, the total number of elements in the Pauli group is 4^n , since each qubit can be X, Y, Z or I independently. Therefore, the complexity of measuring f vastly depends on the form of the target state ρ_f : for a generic ρ_f which contains all $R = 4^n - 1$ Pauli terms (without the identity term), gaining f in experiment via Eq. (5) is equivalent to carrying out full state tomography and thus inefficient; for some other ρ_f , such as the 12-coherence in our experiment which only contains one Pauli term $Z^{\otimes 12}$, $R = 1$ measurement is already sufficient to obtain f . Fortunately, the target states in many quantum computing tasks do not involve exponential number of Pauli terms, i.e. R is polynomial, where our experiment provides an example. In this sense, measuring f is efficient in these tasks. To be explicit, in the r -th experiment, we just apply the control field to the initial state ρ_i and measure the expectation value $\langle P_r \rangle$ of $\tilde{\rho}$.

Measuring g requires to realise the commutator inside Eq. (3), namely $[\sigma_{x,y}^k, \cdot]$. In fact [2],

$$[\sigma_{x,y}^k, \rho] = i \left[\left(\frac{\pi}{2} \right)_{x,y}^k \rho \left(\frac{\pi}{2} \right)_{x,y}^{k \dagger} - \left(-\frac{\pi}{2} \right)_{x,y}^k \rho \left(-\frac{\pi}{2} \right)_{x,y}^{k \dagger} \right], \quad (6)$$

in which $(\pm\pi/2)_{x,y}^k$ is the $\pm\pi/2$ rotation about x or y axis on the k -th qubit. By substituting Eq. (6) into Eq. (3), we get

$$\begin{aligned} g_{x,y}[m] = \frac{\Delta t}{2} \sum_{k=1}^n \text{tr} \left\{ \left[U_M \cdots U_{m+1} \left(\frac{\pi}{2} \right)_{x,y}^k U_m \cdots U_1 \rho_i \left(U_M \cdots U_{m+1} \left(\frac{\pi}{2} \right)_{x,y}^k U_m \cdots U_1 \right)^\dagger - \right. \right. \\ \left. \left. U_M \cdots U_{m+1} \left(-\frac{\pi}{2} \right)_{x,y}^k U_m \cdots U_1 \rho_i \left(U_M \cdots U_{m+1} \left(-\frac{\pi}{2} \right)_{x,y}^k U_m \cdots U_1 \right)^\dagger \right] \rho_f \right\}. \end{aligned} \quad (7)$$

For every term on the right-hand side, it is very similar to the measurement of f in Eq. (2), but with a local $\pi/2$ pulse inserted between slices m and $m + 1$. Explicitly, the m -th component of $g_{x,y}$ is a weighted sum of $4nR$ measurement results, where $4n$ comes from the fact that local $\pi/2$ pulses have four axes and traverse all n qubits, and R is due to the measurement of f . To measure $g_x[m]$, we use $2n$ experiments by inserting $\{(\pm\pi/2)_x^k\}_{k=1,\dots,n}$ at the m th slice evolution. Measuring $g_y[m]$ is analogous. Provided that the qubits are all well individually addressed, high fidelities are attainable in implementing these local rotations.

In total, we need $4nMR$ experiments to perform the gradient measurement, where M is the total number of slices in the control field.

3. Our 12-qubit quantum processor

Our 12-qubit processor is per-¹³C labeled (1S,4S,5S)-7,7-dichloro-6-oxo-2-thiabicyclo[3.2.0]heptane-4-carboxylic acid dissolved in d6-acetone, with the molecular structure shown in Fig. S1. The unlabeled compound was synthesised previously and its structure was established unambiguously by a single crystal X-ray diffraction study [3].

When placed in a static z -magnetic field, this 12-qubit sample has an Ising Hamiltonian of the form

$$\mathcal{H}_s = -\pi \sum_{i=1}^{12} \nu_0^i \sigma_z^i + \frac{\pi}{2} \sum_{i=1 < j}^{12} J_{ij} \sigma_z^i \sigma_z^j, \quad (8)$$

where ν_0^i is the chemical shift of the i th spin, J_{ij} is the coupling between spins i and j , and σ_z^i is the Pauli-z operator of the i th

	C1	C2	C3	C4	C5	C6	C7	H1	H2	H3	H4	H5
C1	30020											
C2	57.58	8779										
C3	-2.00	32.70	6245									
C4	0	0.30	0	10333								
C5	-1.25	2.62	1.11	33.16	15745							
C6	5.54	-1.66	0	-3.53	33.16	34381						
C7	1.25	37.48	0.94	29.02	21.75	34.57	11928					
H1	0	0	2.36	166.6	4.06	5.39	8.61	3310				
H2	4.41	1.86	146.6	2.37	0	0	0	0	2468			
H3	1.81	3.71	146.6	2.37	0	0	0	0.18	-12.41	2158		
H4	-13.19	133.6	-6.97	6.23	0	5.39	3.78	-0.68	1.28	6.00	2692	
H5	7.87	-8.35	3.35	8.13	2.36	8.52	148.5	8.46	-1.06	-0.36	1.30	3649
T ₁	7.99	3.61	1.83	3.72	9.89	7.80	3.64	3.83	2.13	2.28	2.65	3.47
T ₂ [*]	0.40	0.31	0.44	0.25	0.25	0.40	0.38	0.29	0.39	0.34	0.15	0.30

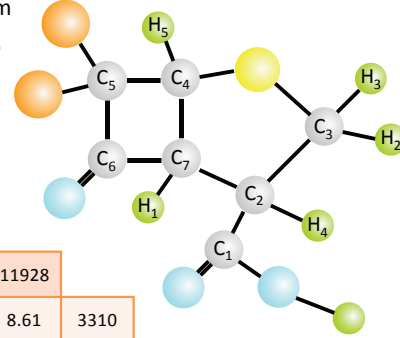


Figure S1. Molecular structure and Hamiltonian parameters of per-¹³C labeled (1S,4S,5S)-7,7-dichloro-6-oxo-2-thiabicyclo[3.2.0]heptane-4-carboxylic acid. C₁ to C₇, and H₁ to H₅ denote the 12 qubits from qubit 1 to qubit 12, respectively. The diagonal elements are the chemical shifts (in Hz), and the off-diagonal elements are the *J*-couplings between two spins (in Hz). The relaxation times T₁ and T₂ (in seconds) are also listed at bottom.

spin. At room temperature, the thermal equilibrium state of this system is highly mixed, with the form

$$\rho_{eq} = \frac{1-\epsilon}{2^{12}} \mathbb{I} + \epsilon \left(\gamma_C \sum_{i=1}^7 \sigma_z^i + \gamma_H \sum_{j=8}^{12} \sigma_z^j \right), \quad (9)$$

where $\epsilon \approx 10^{-5}$ describes the polarization, \mathbb{I} is a $2^{12} \times 2^{12}$ identity matrix, and γ_C and γ_H are the gyromagnetic ratios of the ¹³C and ¹H nuclei, respectively. In particular, $\gamma_H \approx 4\gamma_C$, so the signal of ¹H is roughly four times larger than that of ¹³C. As the large identity part in Eq. (9) does not contribute to the NMR spectrum under unitary evolutions, we just omit it in general and use the remaining term, called deviation density matrix, to represent the state by

$$\rho_{dev} \approx \sum_{i=1}^7 \sigma_z^i + 4 \sum_{j=8}^{12} \sigma_z^j, \quad (10)$$

in which $\gamma_H \approx 4\gamma_C$ is used and the polarization ϵ is dropped. In Fig. S2, the ¹³C and ¹H thermal equilibrium spectra are shown, while the spectra of C₂, C₆, H₃, and H₅ are magnified for better visualization. All 12 spins can be individually addressed by their distinct chemical shifts as shown in Fig. S1. For each spin, the spectrum in principle contains 2^{11} peaks due to its couplings with the other 11 spins, since each coupling splits the peaks of the present spin into two. However, many interactions, especially those between distant spins, are too small to be resolved spectrally, so the number of observable peaks is far less than 2^{11} .

In NMR quantum computing, we often tackle problems in the rotating frame instead of in the lab frame, which is more convenient. For the internal Hamiltonian in Eq. (8), we set the two transmission frequencies as $o_1 = 20,696$ Hz and $o_2 = 2,894$ Hz for the channel ¹³C and ¹H, respectively. The transmission frequencies are chosen as the central frequencies of the spectra. In this double-rotating frame, the internal Hamiltonian becomes

$$\mathcal{H}_s^{rot} = -\pi \sum_{i=1}^7 (\nu_0^i - o_1) \sigma_z^i - \pi \sum_{j=8}^{12} (\nu_0^j - o_2) \sigma_z^j + \frac{\pi}{2} \sum_{i=1 < j}^{12} J_{ij} \sigma_z^i \sigma_z^j, \quad (11)$$

which is a conventional form in NMR quantum computing.

The external control field is applied in the transverse *x*-*y* plane, while oscillating at the transmission frequency of ¹³C and ¹H channel, respectively. These transmission frequencies are in the radio-frequency (r.f.) regime. There are four control parameters,

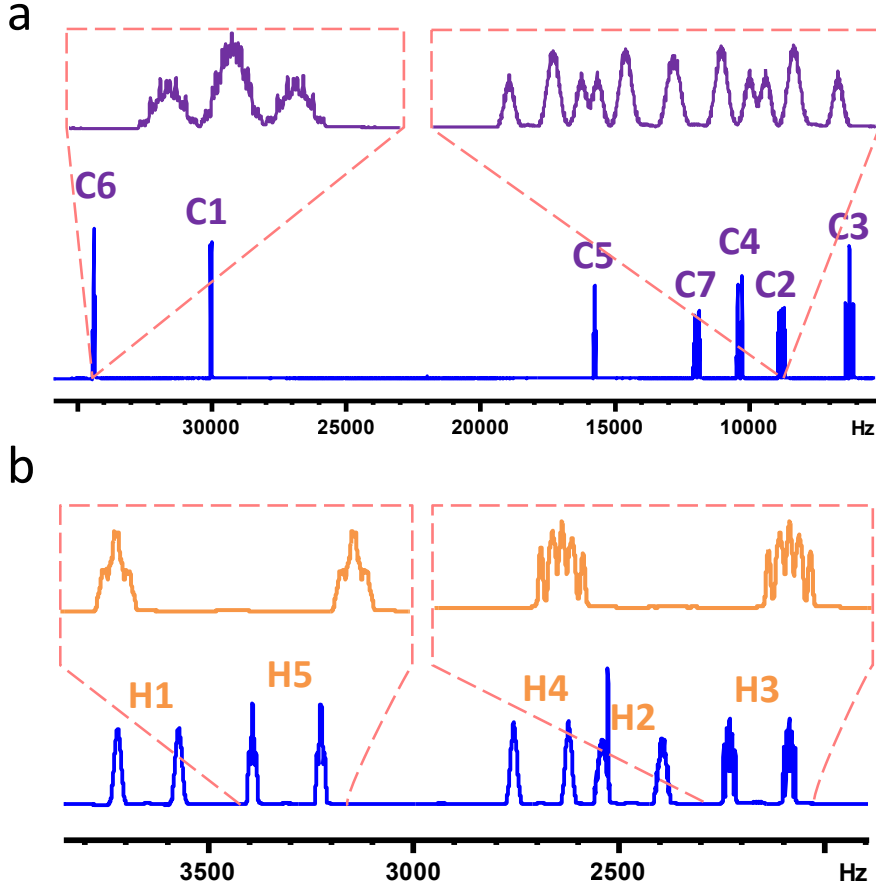


Figure S2. Thermal spectra of **a**, ¹³C and **b**, ¹H in the 12-qubit quantum processor. In particular, the spectra of C₂, C₆, H₃, and H₅ are magnified for better visualization. The *y*-axis represents the signal strength (a.u.). Different spins are individually addressed according to their distinct resonance frequencies, and the spectrum of each spin is split into up to 2¹¹ peaks due to its couplings with the other 11 spins (though many splittings are too small to be resolved).

namely B_x^C, B_y^C, B_x^H, and B_y^H, in a time-independent r.f. pulse, where, without loss of generality, B_x^C means the control field amplitude along *x*-axis for the ¹³C channel. In the double-rotating frame, the Hamiltonian of the external control field is

$$\mathcal{H}_c^{rot} = B_x^C \sum_{i=1}^7 \sigma_x^i + B_y^C \sum_{i=1}^7 \sigma_y^i + B_x^H \sum_{j=8}^{12} \sigma_x^j + B_y^H \sum_{j=8}^{12} \sigma_y^j. \quad (12)$$

Together with the internal Hamiltonian \mathcal{H}_s^{rot} in Eq. (11), the dynamics of the total system is dominated by the joint action of the internal and external Hamiltonians, with the propagator

$$U = e^{-i(\mathcal{H}_s^{rot} + \mathcal{H}_c^{rot})t}. \quad (13)$$

All elementary gates such as single-qubit rotations and two-qubit controlled-NOT (CNOT) gates required in quantum information processing can be realised by deliberately designing the external Hamiltonian [4].

For instance, if we want to realise a $\pi/2$ rotation about the *x*-axis for C₁, denoted as $R_x^1(\pi/2)$, we can use a *M*-slice shaped pulse with slice width Δt . In each slice, the four parameters of the control field are constants, labeled as B_x^C[*m*], B_y^C[*m*], B_x^H[*m*], and B_y^H[*m*], respectively. The propagator of such a shaped pulse is a concatenation of the propagator in Eq. (13)

$$U_{[1]}^{[M]} = U_M U_{M-1} \cdots U_1, \quad \text{with} \quad U_m = e^{-i(\mathcal{H}_s + \mathcal{H}_c[m])\Delta t}, \quad (14)$$

where the notation $U_{[1]}^{[M]}$ means the shaped pulse is applied from the first slice to slice *M*.

The next step is to find the shaped pulse, i.e., a sequence of B_{x,y}^{C,H}[*m*], such that the propagator in Eq. (14) realises the target operation $R_x^1(\pi/2)$ with high fidelity. In state-of-the-art NMR techniques, this optimisation procedure is often realised

Operator	Length	Simulated Fidelity	Number of Slices	Δt
$C_7H_1 - SWAP$	8 ms	99.0%	400	$20 \mu s$
$R_y^{1-6,8-12}(\pi/2)$	1 ms	99.8%	100	$10 \mu s$
$R_y^7(\pi/2)$	1 ms	99.9%	100	$10 \mu s$
$R_x^2(\pi)$	2 ms	99.8%	200	$10 \mu s$
$R_x^6(\pi)$	2 ms	99.8%	200	$10 \mu s$
$R_x^4(\pi)$	2 ms	99.7%	200	$10 \mu s$
$R_x^{5,7}(\pi)$	2 ms	99.8%	200	$10 \mu s$
$R_{-y}^7(\pi/2)$	1 ms	99.9%	100	$10 \mu s$
$R_y^2(\pi/2)$	1 ms	99.9%	100	$10 \mu s$
$R_x^1(\pi)$	2 ms	99.8%	200	$10 \mu s$
$R_x^{2,3}(\pi)$	2 ms	99.8%	200	$10 \mu s$
$R_{-y}^2(\pi/2)$	1 ms	99.9%	100	$10 \mu s$

Table I. Shaped pulse optimised by SSGRAPE during the 12-coherence creation. The pulses are listed in the order of their appearances in Fig. S3. Although the pulses are found with the subsystem method, the fidelities reported here are calculated on the full 12-qubit system.

via the GRAPE algorithm, as a shaped pulse found by GRAPE can have the properties of short duration and robustness to uncertainties in the Hamiltonian, e.g, the inhomogeneity of the static or control field. In small-scale systems with around seven spins, GRAPE is quite powerful, as it generates high-fidelity shaped pulses readily with modern computing power. However, in the 12-qubit system, GRAPE is significantly more challenging, as it requires much higher dimensional matrix multiplications and exponentiating. Therefore, we modified the original GRAPE and applied this algorithm based on subsystems, which we call subsystem-GRAPE (SSGRAPE).

SSGRAPE has the same scalability problem as the original GRAPE, but it does provide a solution to pulse optimisations in a large system. For example, in our 12-qubit system, by artificially disconnecting C_2 and C_7 , we divided the entire system into two subsystems with each consisting of six spins. From Fig. S1 and the relevant parameters, it can be seen that the two subsystems are isolated to a good approximation. We define the subsystem with C_2 as S_A , and the other as S_B . Both internal and external Hamiltonians in S_A and S_B can be determined by tracing out the other subsystem. For a target operator, say $U_{tar} = R_x^1(\pi/2)$, it can be decomposed into two operators

$$U_{tar}^A = R_x^1\left(\frac{\pi}{2}\right), \quad U_{tar}^B = I, \quad (15)$$

where U_{tar}^A and U_{tar}^B are now $2^6 \times 2^6$ unitary operators, and $U_{tar} = U_{tar}^A \otimes U_{tar}^B$. Therefore, the 12-qubit GRAPE optimisation problem can be treated as two 6-qubit problems, and SSGRAPE attempts to optimise a shaped pulse which can realise U_{tar}^A and U_{tar}^B simultaneously. In brief, the SSGRAPE technique greatly reduces the computation time of the pulse finding on our 12-qubit system, but it is worth emphasising that it does not fundamentally solve the scalability issue.

Another requirement of adopting SSGRAPE is that the target unitary operator can be effectively decomposed using subsystems and does not involve interactions between subsystems. In our 12-qubit experiment, this condition holds for every operator. We list all the SSGRAPE-optimised shaped pulses that are needed in the experiment, as shown in Table I. We also simulated the fidelity of each pulse in the full 12-qubit system. That is, each pulse was found using SSGRAPE in the two 6-qubit subsystems, but then simulated on the full system. All local pulses are over 99.7% fidelity in simulation, which demonstrates that SSGRAPE is a valid pulse finding method for our 12-qubit system.

4. Experimental implementation of creating a 7-coherence

In this section, we present a step-by-step description of our experiment to create the $Z^{\otimes 7}I^{\otimes 5}$, and show the relevant NMR spectra after each step.

(a) From the initial state to ρ_a

The whole circuit is depicted in Fig. S3, with four intermediate states labeled by ρ_a to ρ_d . The initial state is the deviation density matrix $\rho_{dev} = \sum_{i=1}^7 Z_i + 4 \sum_{j=8}^{12} Z_j$ of the thermal equilibrium state, as described in Eq. (10). It first undergoes an 8

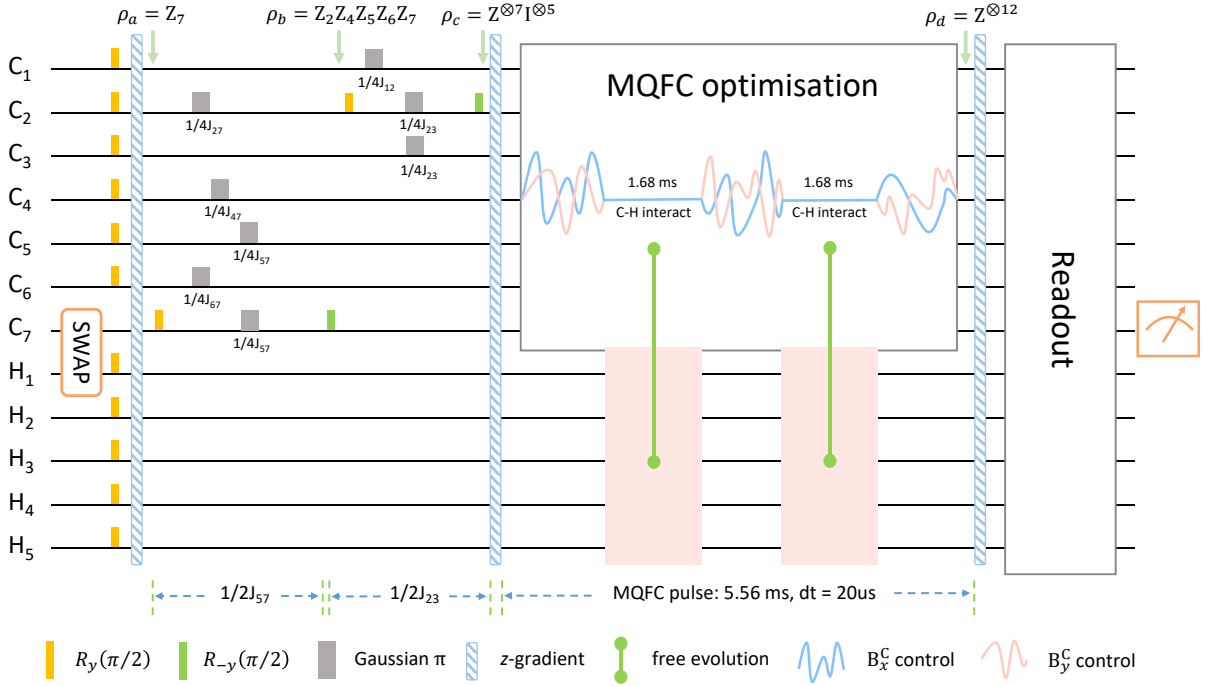


Figure S3. Quantum circuit that evolves the system from thermal equilibrium state to 12-coherence. Four intermediate states ρ_a to ρ_d are marked at the top, which assists in the understanding of the entire circuit. In particular, the MQFC procedure is applied on 7-coherence $Z^{\otimes 7}I^{\otimes 5}$.

ms SWAP gate, whose purpose is to boost the signal of C₇ by approximately four times. In fact, this gate is not strictly a unitary SWAP gate but a state-to-state transformation, which enables C₇ and H₁ to swap their equilibrium spin states. The physics behind it is the nuclear Overhauser effect (NOE) [5]. After that, a multi-qubit rotation about the y -axis on all spins except C₇ is applied to rotate these spins to the transverse plane, followed by a z -direction gradient field. A z -gradient pulse is used to destroy non-zero coherences, i.e. removes all the Pauli terms that include X and Y operators in our case. As all the other spins except C₇ are flipped to the x - y plane, the output state after the gradient is

$$\rho_a = Z_7. \quad (16)$$

Here, we have ignored the factor of four before Z_7 for convenience, as this state will be used as the reference for future calibrations. When we observed C₇ by rotating it to X, the two spectra of ρ_a are plotted in Figs. S4a and S4b. The left one is the spectrum of C₇ in the 12-qubit regime, and the right one is obtained by decoupling the ¹H channel via the Waltz-16 sequence [6]. This decoupling can be considered as a partial trace process, which can remarkably improve the spectrum resolution, but it requires that the state of the five ¹H nuclei is equal to the identity.

(b) From ρ_a to ρ_b

The next step is to create a 5-coherence on the nearest neighbours of C₇, including C₂, C₄, C₅, and C₆. Let us start from a simple example to describe how to increase the coherence order. For two qubits, if we start from XI, choose $t = 1/(2J)$, and let the system evolve under the J -coupling of $\sigma_z\sigma_z$ term (see Eq. (8)), the coherence order of the system can be increased by one due to the fact

$$XI \xrightarrow{U(1/2J)=\pi\sigma_z^1\sigma_z^2/4} YZ. \quad (17)$$

The main idea of creating 5-coherence is to make use of the partial refocusing scheme [7], that only the desired J -coupling evolutions are left to undergo $t = 1/(2J)$ evolutions, while all the unwanted couplings are refocused. Refocusing of an unwanted $\sigma_z\sigma_z$ coupling term can be realised by inserting a π pulse on one spin in the centre of the evolution but no pulse on the other. Although the desired couplings J_{27} , J_{47} , J_{57} , and J_{67} are different, a simultaneous J -coupling evolution is possible by careful design of the π -pulse positions as shown in Fig. S3.

After the partial refocusing sequence and a subsequent $R_y^7(-\pi/2)$ pulse that rotates C₇ back to Z, the ideal state at point b is

$$\rho_b = Z_2Z_4Z_5Z_6Z_7. \quad (18)$$

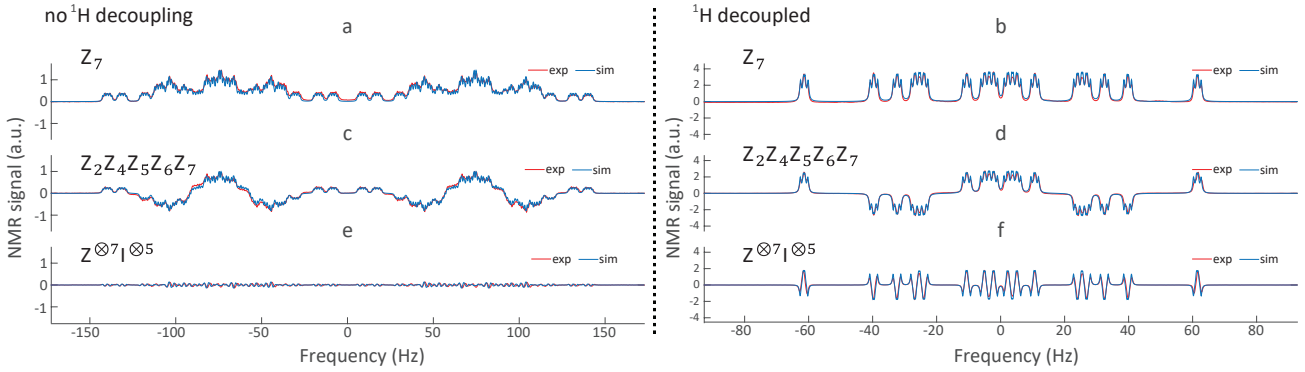


Figure S4. Spectra for the observation of ρ_a (**a**, **b**), ρ_b (**c**, **d**), and ρ_c (**e**, **f**) on C_7 , respectively. The left column is without ^1H decoupling, and the right column is with ^1H decoupled. The spectra in the left column are averaged over 30 scans to gain a good signal-to-noise ratio, while the ones in the right column are averaged over only 10 scans. In each spectrum, the experiment is in strong agreement with simulation, indicating that our control on this 12-qubit system is precise.

In experiment, we observed C_7 for this 5-coherence state, and the two spectra without and with decoupling the ^1H channel are shown in Figs. S4c and S4d, respectively. The signal attenuation in experiment is about 20.7% due to decoherence, so the simulated spectra were rescaled by 1.26 times to fit the experimental data.

(c) From ρ_b to ρ_c

In this step, we create the 7-coherence involving all the ^{13}C nuclei. Coherence is transferred to the remaining C_1 and C_3 spins from their joint neighbour C_2 . Similar to the above procedure, this step also involves a partial refocusing sequence, which realises the $t = 1/(2J)$ evolutions for J_{12} and J_{23} simultaneously. After a local pulse $R_y^2(-\pi/2)$ on C_2 , the state at point *c* is

$$\rho_c = Z^{\otimes 7}I^{\otimes 5}, \quad (19)$$

where $I^{\otimes 5}$ indicates that all five ^1H 's are still in the identity state. The experimental spectra of C_7 without and with ^1H decoupling are plotted in Figs. S4e and S4f, respectively. The simulated spectra were rescaled by 1.42 (compared to the simulated spectra of ρ_a) to make an optimal fit with the experimental result.

Despite the non-negligible decoherence effect during the experimental creation of 7-coherence, we emphasise that this signal attenuation will not impact the characterisation of the MQFC procedure, which is the main focus of this work. As shown in Figs. S4e and S4f, the creation of 7-coherence is remarkably precise up to a rescaling factor. This 7-coherence state can be used as a reference to calibrate the 12-coherence created via MQFC. Hence, the scaling factor of the 7-coherence state is irrelevant. We also direct readers to Ref. [7] for a detailed calibration of our 7-coherence result and the relevant spectrum of another spin C_2 .

5. Experimental MQFC optimisation to create 12-coherence

Here is the central focus of this paper, where we designed a shaped pulse based on MQFC to create 12-coherence from 7-coherence. In the circuit of Fig. S3, it corresponds to the part between ρ_c and ρ_d . Unlike the preceding section where all pulses were calculated by classical SSGRAPE algorithm, the MQFC optimisation is purely quantum, as the fitness function f and gradient g were directly measured on the 12-qubit quantum computer. The only role that a classical computer played during MQFC was to update the control field based on the measured gradient g , which is merely simple algebra without additional time cost. That is, no inefficient calculations on classical computers were required during MQFC.

After the creation of 7-coherence $\rho_c = Z^{\otimes 7}I^{\otimes 5}$, we applied a z -direction gradient field as depicted in Fig. S3. The purpose is to remove unwanted terms produced due to experimental imperfections, since $Z^{\otimes 7}I^{\otimes 5}$ itself is invariant under this gradient field. This technique is conventional in NMR quantum computing to 'clean up' the experimentally prepared input state, and has no influence on the subsequent MQFC procedure.

The structure of the shaped pulse used in MQFC was pre-designed according to the molecular information in Fig. S1. It consists of five parts: three sub-pulses and two free evolutions in between sub-pulses as shown in the *MQFC optimisation* box in Fig. S3. The general idea of this structure design is to let ^{13}C 's interact with five ^1H 's simultaneously and hence increase the coherence order by five. Note that all large C-H couplings in Fig. S1 are not very distinct, roughly $J_{ave} = 148.8$ Hz on average. Therefore, we set the time for the two free evolutions as $1/4J_{ave} \approx 1.68$ ms, and expect that it enables sufficient C-H interaction time to produce higher coherence on the five ^1H 's. As a result, the purpose of placing the three sub-pulses is: the first one is to rotate C_2 , C_3 , C_4 , and C_7 , which are directly connected to ^1H , to the x - y plane; the second sub-pulse is to refocus

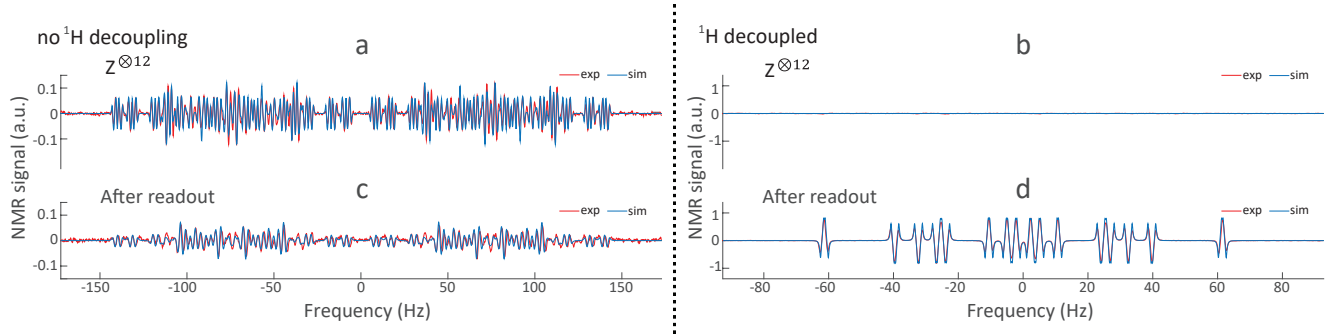


Figure S5. Spectra for the observation of 12-coherence ρ_d (**a**, **b**) and after the readout stage (**c**, **d**) on C₇, respectively. The left column is without ¹H decoupling, and the right column is with ¹H decoupled. The ¹H undecoupled spectra are averaged over 30 scans. As shown in **a**, the direct observation of experimental 12-coherence $\rho_d = Z^{\otimes 12}$ matches remarkably well with the simulation, which demonstrates that we have successfully created 12-coherence using the MQFC pulse. Not surprisingly, the decoupling of ¹H leads to no signal in **b**, since the five ¹H's are no longer identity but $Z^{\otimes 5}$. **c** and **d** are the spectra after the readout stage in Fig. S3, whose purpose is to measure f and g in one scan per experiment.

unwanted couplings during the C-H interaction; the last one is to rotate the relevant spins back to Z. The MQFC pulse is set to be 5.56 ms long with $\delta t = 20 \mu\text{s}$. The total number of slices is thus 278, where 168 of them remain zero as they are utilised for free evolutions. The remaining 110 slices are divided into three parts: 30 for the first sub-pulse, 30 for the second sub-pulse, and 40 for the third sub-pulse. Hence, to measure the gradient g in each iteration, we only need to take these 110 slices into account, which greatly reduces the experimental run-time.

Since MQFC is a gradient-based optimisation procedure, the measurements of f and g are critical. As described in Section 2, measuring f is actually equivalent to measuring the expectation value $\langle Z^{\otimes 12} \rangle$ in the experimental state after applying the trial shaped pulse. This measurement requires only one experiment. Analogously, measuring g also involves the readout of the expectation value $\langle Z^{\otimes 12} \rangle$, with a $\pi/2$ local pulse inserted in the trial shaped pulse (see Fig. 2b in the main text and Eq. (7) in Section 2). This measurement requires $4nM$ experiments, where $n = 7$ because we only need to apply local $\pi/2$ pulse on the seven ¹³C's, and $M = 110$ is the number of slices as described in the preceding paragraph. In total, for one iteration, the experimental time of MQFC is

$$T_{exp} = (4nM + 1)\tau_{exp}, \quad (20)$$

where τ_{exp} is dominated by the delay time between two experiments to reestablish thermal equilibrium. Typically, $\tau_{exp} \approx 5T_1$, implying a 30 s delay between experiments. However, the observation of $Z^{\otimes 12}$ in our 12-qubit system requires about 30 experimental scans to yield a good spectrum with acceptable signal-to-noise ratio (SNR), such as the one in Fig. S5a. Estimated by Eq. (20), this requirement leads to a time cost of over one month per iteration, which is impractical as in this experiment we used nine iterations to achieve a high-fidelity MQFC pulse.

Therefore, we need to improve the SNR of the spectrum in order to reduce the number of scans and thus reduce the experimental time. A traditional way is to decouple ¹H spins, which should enhance the SNR by $2^5 = 32$ times, because the NMR signal per peak attenuates exponentially with the number of interacting spins. However, when the five ¹H's are in $Z^{\otimes 5}$, the decoupling, which in fact traces out ¹H, would lead to no signal on ¹³C as shown in Fig. S5b. In other words, it is necessary to evolve the state of ¹H to $I^{\otimes 5}$ before decoupling. In the experiment, we used a readout pulse, described in the next section, to realize this transformation.

6. Readout sequence for the measurement of f and g

As mentioned above, the direct observation of 12-coherence $Z^{\otimes 12}$ requires about 30 scans to yield a good SNR in the spectrum. Compared to the ¹H decoupled spectrum which merely requires one scan, the experimental time of the undecoupled case is 30 times longer and thus impractical for measuring f and g . This section is to describe our readout technique, which enables the decoupling of ¹H's so that each experiment can be done with only one scan.

A readout sequence (see Fig. S6), computed by classical SSGRAPE, is run just after the MQFC procedure. The phase correction is a z -rotation to compensate for the unwanted chemical shift evolutions during $1/2J_{78}$ time. If the state is $Z^{\otimes 12}$, the five ¹H's will evolve to the identity state after the readout sequence, and the decoupling of ¹H will lead to the C₇ spectrum in Fig. S5d, which can be measured in a single scan. We used Lorentzian fitting to obtain the signal amplitude, and thus the value of $\langle Z^{\otimes 12} \rangle$.

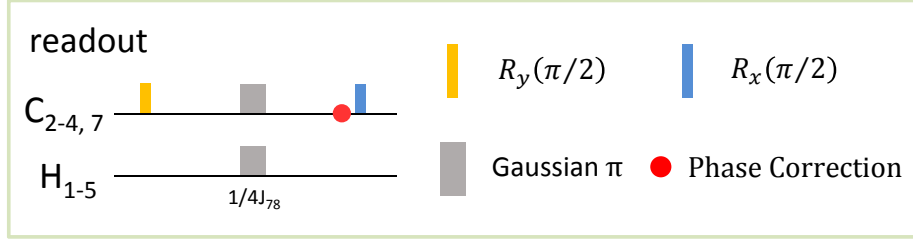


Figure S6. Readout sequence to boost the SNR of the C_7 spectrum. It transforms the 1H spins from Z to identity and thus enables the decoupling of 1H channel. The phase correction compensates for the chemical shift evolutions, after which all relevant spins are along the y -axis. In principle, this technique improves the SNR by a factor of 32, and makes the measurement of f or g practical.

This readout sequence inevitably induced errors in terms of decoherence and pulse imperfections. For the former one, through our simulation we found that the readout caused about 30% signal loss, which is reasonable since multi-coherence is exceptionally vulnerable to decoherence. Therefore, this factor was taken into account for all the measurement results, that is, the measured values are rescaled by 1.3. With respect to the pulse imperfection, it consists of two parts: the imperfection of the sequence itself, i.e. some approximations about J -couplings when designing this simple readout sequence, and the infidelity of the SSGRAPE pulse. In total, 3.5% error arises in simulation, but how the error affects the 12-qubit quantum states is difficult to quantify. We used this value as the uncertainty of the experimental value of $\langle Z^{\otimes 12} \rangle$, namely, the error bars in Fig. 3c in the main text. Fortunately, MQFC outperforms SSGRAPE, even with error bars accounted for, demonstrating that MQFC has the feedback-control property that is able to correct unknown experimental errors.

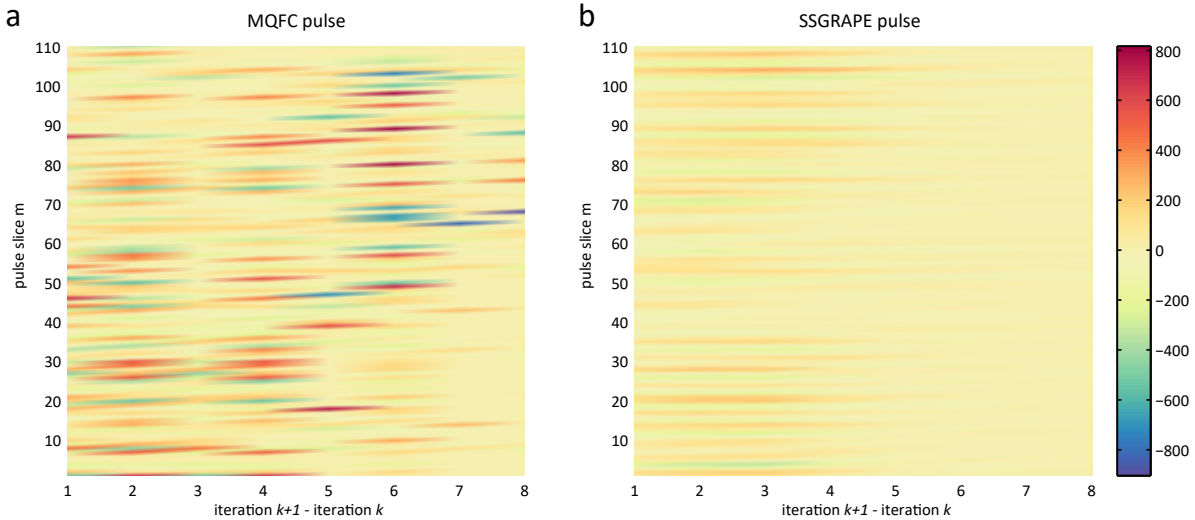


Figure S7. Variations of B_x between iterations $k + 1$ and k , indicated by the x -axis, for **a**, MQFC pulse and **b**, SSGRAPE pulse. The y -axis represents the 110 slices in optimisation (see Section 5), and ΔB_x is plotted in colourscale. Ideally, the two plots should be the same, as MQFC is measuring the gradient information on a quantum computer, which should not be different from the classical SSGRAPE calculations using Eq. (3). Experimentally, however, they are seen to differ. This reflects the unknowns in the experimental system (uncertainties in the Hamiltonian, control fields, etc.), and demonstrates that MQFC is able to correct for these unknowns.

In addition, we plotted the variations of B_x between two iterations for both MQFC and SSGRAPE pulses in Fig. S7. ΔB_x is proportional to the measured g_x (see Eq. (4), and note the $\Delta t/2 = 10 \mu s$ factor in the form of g_x in Eq. (7)), computed by $\Delta B_x = \epsilon g_x$, where ϵ is a fixed step size. In experiment, we chose $\epsilon = 1.6e7$ according to the knowledge gained in SSGRAPE calculation. Note that ϵ can also be efficiently altered using a quadratic fit process, which is a potential improvement of the current experiment by speeding up the convergence of the optimisation procedure. The difference of ΔB_x in Fig. S7a and S7b reflects that unknowns in the experimental system (uncertainties in the Hamiltonian, control fields, etc.) are automatically accounted for by MQFC, confirming its feedback control property.

It is worth stressing that the readout technique used in our experiment is merely to reduce the time cost in measuring f and g . For other systems in which the signal is not exponentially decreased with the growing number of qubits, this readout stage is not necessary. Even in NMR, if we can shorten the equilibration time between two experiments, a greater number of scans can

be tolerated. Preliminary progress has been made towards this goal in our recent work [8].

- [1] Navin Khaneja, Timo Reiss, Cindie Kehlet, Thomas Schulte-Herbrüggen, and Steffen J Glaser. Optimal control of coupled spin dynamics: design of nmr pulse sequences by gradient ascent algorithms. *Journal of Magnetic Resonance*, 172(2):296–305, 2005.
- [2] Jun Li, Xiaodong Yang, Xinhua Peng, and Chang-Pu Sun. Physical realization of a quantum oracle machine. *arXiv:1608.00677*, 2016.
- [3] Jarrod W Johnson, Darryl P Evanoff, Marc E Savard, Gerald Lange, Timothy R Ramadhar, Abdeljalil Assoud, Nicholas J Taylor, and Gary I Dmitrienko. Cyclobutanone mimics of penicillins: effects of substitution on conformation and hemiketal stability. *J. Org. Chem.*, 73(18):6970–6982, 2008.
- [4] Lieven MK Vandersypen and Isaac L Chuang. Nmr techniques for quantum control and computation. *Rev. Mod. Phys.*, 76(4):1037, 2005.
- [5] Horst Frieboe and Jack K Becconsall. *Basic one- and two-dimensional NMR spectroscopy*. VCH Weinheim, 1993.
- [6] AJ Shaka, James Keeler, and Ray Freeman. Evaluation of a new broadband decoupling sequence: Waltz-16. *J. Magn. Reson.*, 53(2):313–340, 1983.
- [7] Dawei Lu, Hang Li, Denis-Alexandre Trottier, Jun Li, Aharon Brodutch, Anthony P Krismanich, Ahmad Ghavami, Gary I Dmitrienko, Guiliu Long, Jonathan Baugh, et al. Experimental estimation of average fidelity of a clifford gate on a 7-qubit quantum processor. *Phys. Rev. Lett.*, 114(14):140505, 2015.
- [8] Jun Li, Dawei Lu, Zhihuang Luo, Raymond Laflamme, Xinhua Peng, and Jiangfeng Du. Approximation of reachable sets for coherently controlled open quantum systems: Application to quantum state engineering. *Phys. Rev. A*, 94:012312, 2016.